

Alma Mater Studiorum Università di Bologna  
Archivio istituzionale della ricerca

Impact of sedimentation, climate and sea level on marine sedimentary pyrite sulfur isotopes: Insights from the Valle di Manche section (Lower-Middle Pleistocene, southern Italy)

This is the submitted version (pre peer-review, preprint) of the following publication:

*Published Version:*

Houghton J., Scarponi D., Capraro L., Fike D.A. (2022). Impact of sedimentation, climate and sea level on marine sedimentary pyrite sulfur isotopes: Insights from the Valle di Manche section (Lower-Middle Pleistocene, southern Italy). *PALAEOGEOGRAPHY PALAEOCLIMATOLOGY PALAEOECOLOGY*, 585, 1-13 [10.1016/j.palaeo.2021.110730].

*Availability:*

This version is available at: <https://hdl.handle.net/11585/845582> since: 2022-01-14

*Published:*

DOI: <http://doi.org/10.1016/j.palaeo.2021.110730>

*Terms of use:*

Some rights reserved. The terms and conditions for the reuse of this version of the manuscript are specified in the publishing policy. For all terms of use and more information see the publisher's website.

This item was downloaded from IRIS Università di Bologna (<https://cris.unibo.it/>).  
When citing, please refer to the published version.

(Article begins on next page)

This is the final peer-reviewed accepted manuscript of:

Houghton J.; Scarponi D.; Capraro L.; Fike D. A.: Impact of sedimentation, climate and sea level on marine sedimentary pyrite sulfur isotopes: Insights from the Valle di Manche section (Lower-Middle Pleistocene, southern Italy). PALAEOGEOGRAPHY PALAEOCLIMATOLOGY PALAEOECOLOGY, 585. ISSN 0031-0182

DOI: 10.1016/j.palaeo.2021.110730

The final published version is available online at:

<http://dx.doi.org/10.1016/j.palaeo.2021.110730>

Rights / License:

The terms and conditions for the reuse of this version of the manuscript are specified in the publishing policy. For all terms of use and more information see the publisher's website.

*This item was downloaded from IRIS Università di Bologna (<https://cris.unibo.it/>)*

***When citing, please refer to the published version.***

# Impact of sedimentation, climate and sea level on marine sedimentary pyrite sulfur isotopes: Insights from the Valle di Manche section (Lower-Middle Pleistocene, southern Italy)

J. Houghton<sup>a,\*</sup>, D. Scarponi<sup>b</sup>, L. Capraro<sup>c</sup>, D.A. Fike<sup>a</sup>

<sup>a</sup> Earth and Planetary Sciences, Washington University in St. Louis, St. Louis, MO, USA

<sup>b</sup> Dipartimento di Scienze Biologiche Geologiche e Ambientali, University of Bologna, Piazza di Porta San Donato 1, 40126 Bologna, Italy

<sup>c</sup> Dipartimento di GeoScienze, University of Padua, via G. Gradenigo, 6, 40126 Padua, Italy

## ARTICLE INFO

### Keywords:

Sulfur cycling

Chemostratigraphy

Paleoenvironmental reconstruction

Depositional environment

Sequence stratigraphy

## ABSTRACT

Variations in the isotopic composition of sulfur in sedimentary pyrite ( $\delta^{34}\text{S}_{\text{pyr}}$ ) are often used to reconstruct global sulfur biogeochemical cycling and Earth's surface oxidation state over Earth history. Recent work, however, has shown that  $\delta^{34}\text{S}_{\text{pyr}}$  is strongly impacted by local depositional conditions, which both confounds attempts to reconstruct global sulfur cycling and provides a new proxy for investigating local paleoenvironmental conditions. We present a chemostratigraphic record of  $\delta^{34}\text{S}_{\text{pyr}}$  in a detailed paleoenvironmental and sequence stratigraphic framework spanning the Early-Mid Pleistocene transition from the Croton Basin (Calabria, Southern Italy). Bulk  $\delta^{34}\text{S}_{\text{pyr}}$  data parallel transgressive-regressive cycles and enable the differentiation of progradational and retrogradational stacking patterns, where  $\delta^{34}\text{S}_{\text{pyr}}$  values decrease toward  $-50\text{‰}$  in outer shelf deposits during late transgression and become more positive and variable in prograding sedimentary units accumulated in shallower environments. In parallel with the observed variations in  $\delta^{34}\text{S}_{\text{pyr}}$ , complementary data on organic carbon abundance and isotopic composition and total nitrogen abundance document changes in terrestrial delivery of sediment to the basin, as a consequence of glacial-interglacial eustatic sea-level changes, regional climate and local tectonics. The chemostratigraphic record of  $\delta^{34}\text{S}_{\text{pyr}}$  appears sensitive to variations in sedimentation rates and local erosional surfaces and therefore may represent a powerful tool to assess stratal stacking patterns for sequence stratigraphic interpretations of siliciclastic successions. These results highlight the role of local conditions in controlling sedimentary  $\delta^{34}\text{S}_{\text{pyr}}$  records and illustrate how isotopic data can be used to reconstruct key parameters of the sedimentary environment that might not otherwise be accessible, especially in deep-time strata.

## 1. Introduction

Sedimentary pyrite ( $\text{FeS}_2$ ) forms as a result of reaction of dissolved Fe(II) or Fe(III)-bearing solids with hydrogen sulfide, predominantly sourced from microbial sulfate reduction (MSR) (Berner, 1978; Goldhaber and Kaplan, 1980; Rickard and Luther, 2007; Wan et al., 2017). The formation and subsequent burial of pyrite is the main sink of reduced sulfur from the ocean, and together with organic carbon burial, contributes to the maintenance of an oxidized Earth surface (Berner, 1984; Garrels and Lerman, 1984). The isotopic composition of sulfur in pyrite ( $\delta^{34}\text{S}_{\text{pyr}}$ ) primarily reflects an offset from the coexisting porewater sulfate pool in sediments where pyrite forms due to the preferential

reduction of  $^{32}\text{S}$  relative to  $^{34}\text{S}$  during MSR. Pyrite preserved in sediments is thought to retain the stable isotopic composition of its hydrogen sulfide source with minimal offset during precipitation (Price and Shieh, 1979). As such,  $\delta^{34}\text{S}_{\text{pyr}}$  can act as a proxy for the  $\delta^{34}\text{S}_{\text{SO}_4}$  of seawater (albeit variably offset by microbial fractionation) when pore fluids remain hydraulically connected to the overlying water column (Canfield, 2001). In such cases (e.g., deep ocean settings), the  $\delta^{34}\text{S}_{\text{pyr}}$  record can be used to reconstruct ambient microbial sulfur biogeochemical cycling (e.g., Canfield and Teske, 1996), especially in deposits where  $\delta^{34}\text{S}_{\text{SO}_4}$  of seawater is independently known. Within this framework, stratigraphic variations in pyrite sulfur isotopes in ancient deposits are often interpreted to reflect temporal changes in global sulfur

\* Corresponding author.

E-mail addresses: jhoughton@levee.wustl.edu (J. Houghton), daniele.scarponi@unibo.it (D. Scarponi), luca.capraro@unipd.it (L. Capraro), dfike@levee.wustl.edu (D.A. Fike).

cycling (assuming constant microbial fractionation), such as periods of enhanced pyrite precipitation and burial and/or changes in the size of the marine sulfate reservoir (Bernier and Raiswell, 1983; Hurtgen et al., 2005; Yan et al., 2009; Hammarlund et al., 2012). One such example is found in strata associated with the late Ordovician Hirnantian glaciation. Here, positive excursions in the  $\delta^{34}\text{S}_{\text{pyr}}$  record are found in strata across the globe (Yan et al., 2009; Zhang et al., 2009; Gorjan et al., 2012; Hammarlund et al., 2012; Jones and Fike, 2013), seeming to provide strong evidence for a global perturbation to the S biogeochemical cycle. However, no parallel variation in the  $\delta^{34}\text{S}_{\text{SO}_4}$  record is found in these strata (Jones and Fike, 2013), arguing for a local control on these pyrite records attributed to global sea-level change during the onset and termination of glaciation. Similarly, recent observations of large  $\delta^{34}\text{S}_{\text{pyr}}$  variability on temporal scales too rapid to reflect changes in the global sulfur cycle raise concerns regarding the utility of pyrite as a record of global S cycling (Pasquier et al., 2017; Liu et al., 2019). Large and systematic  $\delta^{34}\text{S}_{\text{pyr}}$  variations at the temporal scale of glacial-interglacial cycles (i.e., 100 kyr) observed in shelf environments were demonstrated to be forced by sea-level-driven changes in sedimentation rate (Pasquier et al., 2017). Additional pyrite formation that occurs after deposition, during early diagenesis or late-stage alteration may overprint any primary signature acquired during deposition that could be related to seawater  $\delta^{34}\text{S}_{\text{SO}_4}$  and/or be used to infer microbial metabolic fractionation. However, because diagenetic pyrite formation can be influenced by additional basin-scale or localized syndepositional environmental conditions, the variability in this cumulative signal may allow the extraction of additional environmental signals from the  $\delta^{34}\text{S}_{\text{pyr}}$  record associated with higher frequency sedimentological or stratigraphic cycles.

In the modern ocean, sedimentary pore water  $\delta^{34}\text{S}_{\text{H}_2\text{S}}$  values depend on a variety of physical and biological variables (Claypool, 2004; Wing and Halevy, 2014). Microbial sulfate reduction can induce large isotopic offsets (up to  $\sim 72\%$ ) between sulfate and the  $\text{H}_2\text{S}$  produced (Kaplan and Rittenberg, 1964; Canfield, 2001; Detmers et al., 2001; Sim et al., 2011; Leavitt et al., 2013). This isotopic selectivity (i.e., biological fractionation) depends on various factors, including microbial species, organic substrate utilized and sulfate concentration, and is generally observed to increase as cell-specific sulfate reduction rates decrease (Sim et al., 2011). One primary factor influencing the rate of sulfate reduction is the supply of labile organic matter buried in sediments (Bernier, 1980). Marine biomass (e.g., phytoplankton) is thought to be more bioavailable than detrital terrestrial organics for microorganisms in marine sediments (Mollenhauer and Eglinton, 2007), but can also be rapidly consumed by aerobic respiration prior to reaching the sulfidic zone below the sediment-water interface (Cowie and Hedges, 1994). Thus, while nearshore environments generally have increased input of terrestrial organic matter, it is generally thought to be more refractory due to pre-transport degradation on land (Hedges et al., 2000). Therefore, both total organic carbon (TOC) and its source (marine vs. terrestrial) are potentially important factors that influence the sulfate reduction rate within sediments (Goldhaber and Kaplan, 1975; Toth and Lerman, 1977).

As progressive sulfate reduction consumes porewater sulfate (beyond the resupply provided by diffusion of sulfate into the sediments), the cumulative  $\delta^{34}\text{S}_{\text{H}_2\text{S}}$  value is driven toward the initial starting composition of sulfate, a distillation process that depends on the overall connectivity of the porewater to the overlying water column (Goldhaber and Kaplan, 1975; Jørgensen, 1979; as reviewed in Fike et al., 2015). Physical parameters that influence the isotopic enrichment of the sulfide pool include sedimentation rate (Bernier, 1978) as well as porosity, grain size, lithology, and any sediment reworking/remobilization (e.g., by bioturbation or mixing from storms or wave action). In general, high sedimentation rates more effectively isolate the sediments from the overlying water column and fuel greater sulfate reduction by rapidly burying organic carbon below the oxic zone, leading to  $^{34}\text{S}$ -

enriched porewater sulfide (Claypool, 2004). In contrast, very low sedimentation rates (e.g., in outer shelf environments) allow greater diffusion of oxygen (and sulfate) into sediments, which promotes oxidation of organic carbon by aerobic heterotrophs. Therefore, in sediment-starved environments, the position of the chemocline is deeper, suppressing the activity of sulfate reducers, and resulting in incomplete consumption of sulfate and limited isotopic enrichment in porewaters (Claypool, 2004). As a result, these sediment regimes can influence both sulfate reduction rates and the degree of distillation that either enhance or diminish the apparent biological fractionation recorded in the  $\delta^{34}\text{S}_{\text{pyr}}$  record.

The supply of reactive iron within sediments also contributes to sulfide sequestration in the sedimentary record (i.e., formation of pyrite). The availability of reduced Fe to precipitate pyrite depends on complex redox chemistry within the sediments that will be affected by many environmental factors, including organic carbon loading and sediment source. The depositional parameters contributing to the isotopic composition of the sulfide pool in sediment porewaters, likewise influence the availability of reactive Fe oxides, rates of microbial aerobic respiration, sulfate reduction, and Fe reduction (Goldhaber and Kaplan, 1975) and potential aeration processes such as bioturbation, wave action, and storm events (Aller et al., 1986; Canfield and Raiswell, 1992). In addition, several distinct mechanisms of pyrite formation are recognized that variably depend on intermediate sulfur redox phases such as polysulfide and elemental sulfur (Rickard and Luther III, 1997; Rickard and Luther, 2007), precursor minerals such as mackinawite (Sweeney and Kaplan, 1973; Rickard and Luther, 2007; Risgaard-Petersen et al., 2012), and/or reactive surfaces on Fe oxides (Wan et al., 2017; Peiffer et al., 2015). Thus, the extent and timing of pyrite formation in sediments will depend on complex feedbacks between biotic and abiotic factors during deposition, potentially overprinted by early diagenetic processes, capturing a cumulative but possibly discontinuous record of microbial sulfur cycling. By reconstructing the history of environmental drivers that influence both the formation and isotopic composition of pyrite, including sediment accumulation rate, sediment source (e.g., organic carbon and Fe oxide supply), and physical disturbance in different environments of deposition, the impact of sedimentary processes on the bulk  $\delta^{34}\text{S}_{\text{pyr}}$  representing the net result of in-situ geochemical processes can be assessed. In this contribution we seek to investigate the role of depositional facies and stratigraphic architecture, dictated by both glacial-interglacial changes in sea level and local tectonic activity, on the  $\delta^{34}\text{S}_{\text{pyr}}$  record preserved in the sedimentary succession of Valle di Manche (Crotone Basin, Italy), a Mediterranean reference section for the Middle Pleistocene (Capraro et al., 2017).

## 2. Geologic context

The Crotone Basin (CB) is located in the central-eastern part of the Calabria region, Southern Italy (Fig. 1). It contains a very thick ( $> 3000$  m) and well-exposed marine sedimentary succession spanning from the Middle Miocene to the Middle Pleistocene (Massari et al., 2002, 2010; Capraro et al., 2006, 2011; Zecchin et al., 2013; Macrì et al., 2014). Deposition in the CB is controlled by a strong interplay between regional tectonic activity, climate and magnitude of eustatic sea-level change (Massari et al., 2010 and references therein). The sedimentary succession of the CB was subdivided by Roda (1964) into three tectono-stratigraphic sequences (i.e., Serravallian to early Messinian; middle Messinian to Early Pliocene, Middle Pliocene to Middle Pleistocene). These sequences are bounded by major unconformities, which point to episodes of deformation and basin reorganization in response to the development of both the Apennines and the Calabrian Arc during the Neogene (Rossi and Sartori, 1981; Barone et al., 1982; Van Dijk and Okkes, 1991; Van Dijk, 1992). The CB is further subdivided into small sub-basins, which developed independently and therefore preserve dif-

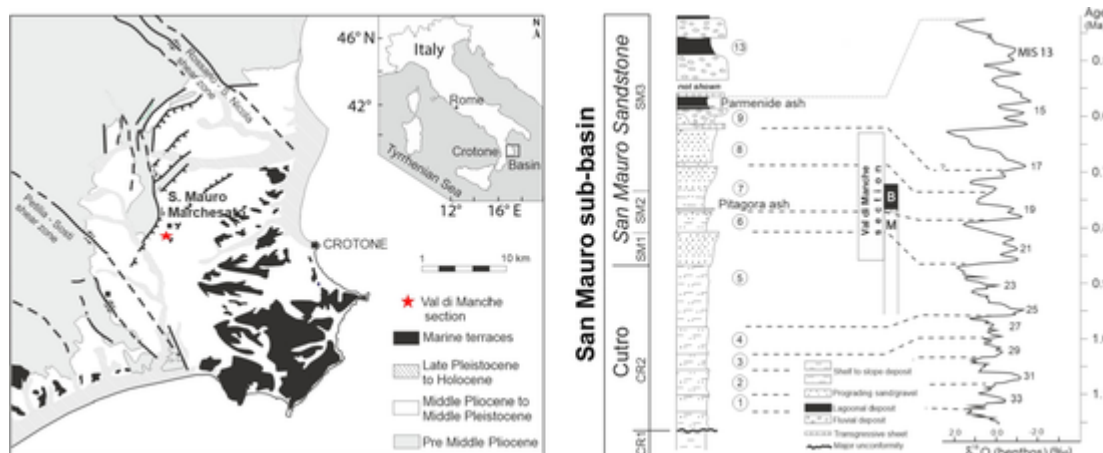


**Fig. 1.** Location and stratigraphic sketch map of the Crotona Basin and the San Mauro (SM) sub-basin (after Massari et al., 2002). (B) The SM cyclic succession and correlation to Marine Isotope Stages (MIS numbers indicated in the  $\delta^{18}\text{O}$  (benthos) curve; after Massari et al., 2002) and subdivision in component units (Cr1–2; SM1–3) of the Cutro and the San Mauro Sandstone formations are sketched along with the stratigraphic position of the Val di Manche section hosting the Matuyama–Brunhes geomagnetic reversal (mid MIS 19). B: Brunhes chron; M: Matuyama chron.

ferent stratigraphic successions (Massari et al., 2010 and references therein).

Our investigation was centered on the San Mauro sub-basin (Rio et al., 1996), which became isolated during the Early Pleistocene in response to the pervasive tectonic activity associated with regional uplift (Fig. 1; Roda, 1964; Massari et al., 2010; Capraro et al., 2011). The younger infill of the San Mauro sub-basin is represented by the San Mauro Sandstone (SMS; Roda, 1964; Rio et al., 1996), which preserves a remarkably continuous and expanded record of the Lower to Middle Pleistocene transition (Rio et al., 1996; Massari et al., 2002, 2007; Capraro et al., 2005, 2015, 2017, 2019). The SMS, which only occurs within the San Mauro sub-basin, was further subdivided by Rio et al. (1996) into three well-recognizable sub-units (Capraro et al., 2015, 2017). From the bottom up, these are: the basal SM1 unit, a prograding package of shallow-water, coarse-grained sands locally rich in the bivalve *Arctica islandica*; the SM2 unit, an overall transgressive package of shelf deposits; and the upper SM3, composed of sandy shoreface and fluvial deposits documenting the final uplift of the area. Altogether, the complex stratigraphic architecture of the SMS demonstrates that sedimentation was controlled by a strong interplay between regional tectonics, eustatic sea-level changes and sediment supply (Rio et al., 1996; Massari et al., 2002, 2007).

Samples investigated for this work were collected in the well-known Valle di Manche (VdM) section (39°05'37.43"N – 16°55'13.94"E), which crops out in the badlands immediately below the village of San Mauro Marchesato (Fig. 1). The VdM section represents the most continuous, expanded and best exposed record of the SMS (Roda, 1964; Rio et al., 1996; Capraro et al., 2015, 2017). In particular, our study focuses on the cyclothem SM2 unit (sequences 6 and 7 of Massari et al., 2007 and references therein), which contains the only known record of the last geomagnetic reversal (i.e. the Matuyama/Brunhes–M/B, boundary; Fig. 1) in the entire Mediterranean marine stratigraphy exposed on land (Macri et al., 2018). The stratigraphic log for the investigated interval (Fig. 2) shows a closely spaced, yet consistent, alternation of facies (Table 1) that point to repetitive (cyclical) changes in stratal stacking patterns (i.e., transgressive-regressive (T-R) cycles). In general, deposition of the SM2 unit occurred during a period of increased subsidence within the San Mauro sub-basin, when the creation of accommodation space exceeded the counter effects of sediment yield and eustasy (Massari et al., 2002, 2007). Still, different thicknesses of individual sedimentary cycles within the SM2 unit indicate that a sharp boost in local subsidence rates occurred after Marine Isotope Stage (MIS) 21, resulting in a very expanded record of sequence 7 (including MIS 19 and the M/B boundary; Massari et al., 2007; Scarponi et al., 2014; Capraro

et al., 2015, 2017). The uplift of the northern and western side of San Mauro sub-basin led to deltaic progradation in the study area and a shift toward marginal marine conditions prior to the generalized uplift of the study area (Massari et al., 2002). Units deposited during full glacial conditions were only sampled in this study from sequence 6, as the sedimentary record deposited during the glacial interval in the overlying younger deposits of sequence 7 rapidly becomes very steep and inaccessible, and dominated by very shallow environments with fluvial incision (braided river gravel deposits) of underlying marine strata during successive sea-level lowstands (Massari et al., 2002, 2007).

## 2.1. Reconstructing paleoenvironment

We analyzed 139 sediment samples, independent of lithology, spanning 36.5 m of stratigraphy with a regular sampling interval of 25 cm, from the same sample set described in Capraro et al. (2015), corresponding to the interval between 867 and 740 ka according to the chronology of Capraro et al. (2017). Prior to any sampling effort, a careful survey of the targeted sedimentary succession was made, and weathered outcrop surface was removed whenever encountered. In addition, detailed descriptions from the VdM section concerning sedimentary facies and sedimentology (Capraro et al., 2017 and references therein), macrofossil and ostracod assemblages (Scarponi et al., 2014 and Rossi et al., 2018, respectively) and pollen records (Capraro et al., 2005) have been combined here to provide a paleoenvironmental framework to interpret the geochemical dataset in this study. Previous work on the San Mauro sub-basin established the physical and sequence stratigraphies for the VdM section across two glacial-interglacial cycles (MIS 21–18, as defined by the reconstructed  $\delta^{18}\text{O}$  record of the benthic foraminifera *Uvigerina peregrina* in Capraro et al., 2017). The transitions between transgressive and regressive stratal stacking patterns and their stratigraphic relations were first established (e.g., Massari et al., 2002, 2007) and later refined using paleoenvironmental reconstructions from macrofaunal and ostracod fossil assemblages (Scarponi et al., 2014; Rossi et al., 2018). The age model used here (Table S1) combines chronostratigraphic control points identified in the same sample suite and reported in Capraro et al. (2017) and Azzarone et al. (2018), both of which were based on the  $\delta^{18}\text{O}$  stack of Wang et al. (2010). Average net sedimentation rates were calculated between control points, which were typically available at ~1 m resolution or better throughout the section (Table S1). This information is illustrated in a stratigraphic log included for reference in Fig. 2 and described in detail in Table 1, which

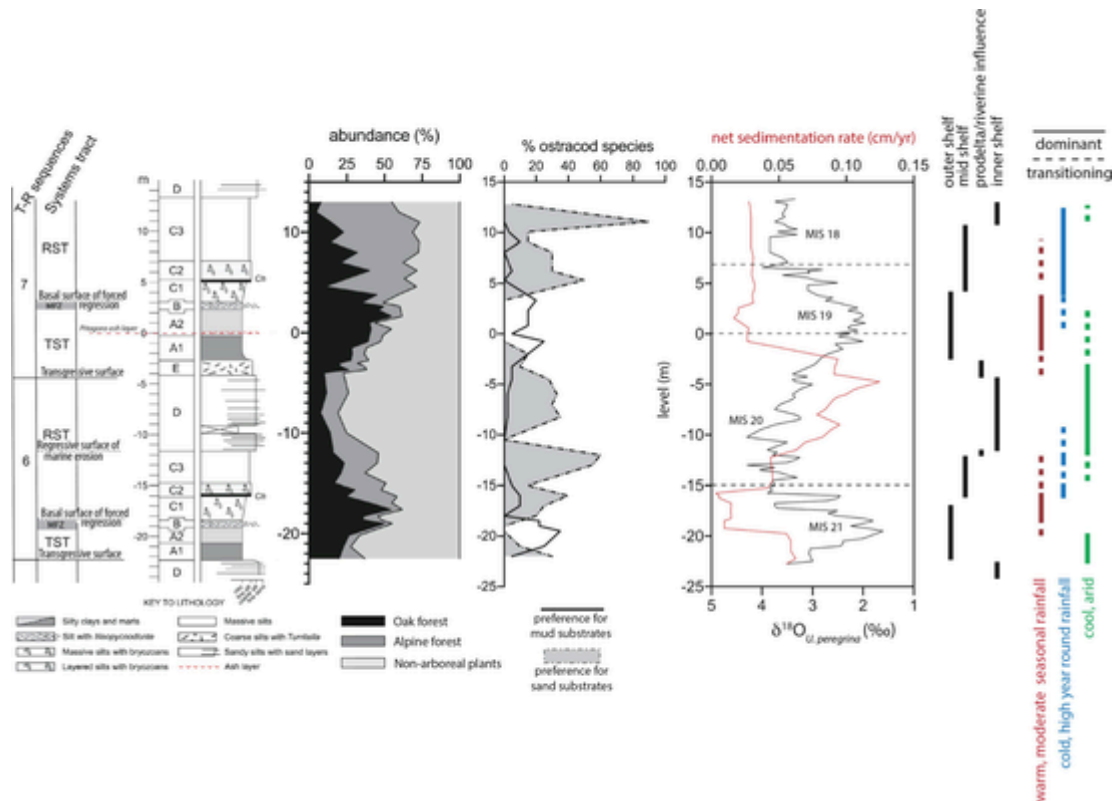


**Fig. 2.** Compilation of paleoenvironmental proxies in the context of the stratigraphy and relevant sequence stratigraphic units and surfaces from the literature (Massari et al., 2007; Rossi et al., 2018) with facies boundaries and descriptions retained from Capraro et al. (2017). The zero datum was placed at the Pitagora ash layer (red dashed line). The simplified pollen record is adapted from Capraro et al. (2005; Figure 9) and the inferred climate transitions from these data are indicated with colored bars (rightmost panel). Relative abundances of ostracod species preferring muddy or sandy substrates is from Rossi et al. (2018) and together with paleoenvironmental information reported in Scarponi et al. (2014) and Capraro et al. (2017) are used to define the general depositional environment (shown in black bars). The  $\delta^{18}\text{O}_{U. peregrina}$  and correlation to MIS units (boundaries indicated with dashed lines) is from Capraro et al. (2017). Age dates reported in Capraro et al. (2017) and Azzarone et al. (2018) were used to calculate the intervening sediment accumulation rates (red line). Abbreviations: MIS = marine isotope stage, T-R = transgressive – regressive sequence, TST = transgressive systems tract, RST = regressive systems tract. (For interpretation of the references to colour in this figure legend, the reader is referred to the web version of this article.)

highlights specific horizons of paleoenvironmental turnover from the combined paleobiologic and lithologic records.

### 3. Methods

#### 3.1. Bulk sulfur isotope analysis

Pyrite sulfur was extracted from acid-insoluble residues (to remove carbonates) using the chromium-reduction method (Canfield et al., 1986). This method allows recovery of all reduced sulfur present in sedimentary samples (primarily pyrite). Samples (~0.5 g) were pre-treated in sequential acidification steps: 10 mL of 6 N HCl was added, slurries were vortexed, centrifuged and supernatant removed. This process was repeated at least three times until no effervescence from carbonate dissolution was visible before triple rinsing with deionized water and drying. Samples remained in contact with acid for less than 30 min to prevent excessive pyrite oxidation or leaching. During the pyrite extraction, acid-insoluble residues were reacted with ~25 mL of 1 M reduced chromium chloride ( $\text{CrCl}_2$ ) solution and 25 mL of 6 N HCl for four hours in a specialized extraction line under a  $\text{N}_2$  atmosphere. The liberated hydrogen sulfide was reacted in a silver nitrate (0.1 M) trap, recovering the sulfide as  $\text{Ag}_2\text{S}$ . Precipitated  $\text{Ag}_2\text{S}$  was rinsed three times using Milli-Q water, and then centrifuged, dried, and homogenized prior to analysis. For analysis, ~350  $\mu\text{g}$   $\text{Ag}_2\text{S}$  was loaded into tin capsules with excess  $\text{V}_2\text{O}_5$ . The  $^{34}\text{S}/^{32}\text{S}$  ratio was measured on a Thermo Delta V Plus, following combustion in a Costech ECS 4010 Elemental Analyzer at Washington University in St. Louis. Pyrite sulfur isotope compositions

are expressed in standard delta notation as permil (‰) deviations from the Vienna Canyon Diablo Troilite (VCDT) standard. Isotopic measurements were calibrated using 3 in-house standards that have been calibrated against international standards IAEA-S-1 (−0.3‰; Robinson, 1995), IAEA-S-3 (−32.5‰; Mann et al., 2009), and NBS-127 (+21.1‰; Coplen et al., 2002). Measurement uncertainty was monitored throughout the analyses using check standards with well-characterized isotopic compositions:  $\text{Ag}_2\text{S}$  (0.3‰ ± 0.35),  $\text{BaSO}_4$  (+14.5‰ ± 0.33), and  $\text{ZnS}$  (−5.5‰ ± 0.55). Precision was determined to be ±0.41‰ based on repeat analyses of check standards and sample replicates. Accuracy was determined to be ±0.48‰ based on the difference between the observed and known values of the check standards and the long-term standard deviations of these check standards (after the methods in Szpak et al., 2017).

#### 3.2. Organic carbon isotope analysis

Sediments were hand crushed to disaggregate prior to chemical analyses. The carbonate mineral fraction was removed from bulk powders (~2 g) using multiple (at least three) short (< 30 min) digestions in 6 N HCl until no effervescence was observed after vortexing. Total dissolution residues were immediately rinsed with distilled water until the supernatant pH was neutral (at least three times), centrifuged, and then completely dried at 50 °C. Carbonate abundance (wt%) was determined gravimetrically by difference. Acid-insoluble residual powders were homogenized and ~10 mg of sample was loaded into tin capsules for organic carbon analyses. Abundance (wt% in original sediment) and

**Table 1**

Description of paleoenvironments from compiled published datasets (see text, Fig. 2) with relevant stratigraphic and lithofacies boundaries/units. The stratigraphic level of internal facies subdivisions is indented and denoted in italics. SSP = stratal stacking pattern, transgressive-regressive depositional sequence from Rossi et al. (2018).

	SSP	Paleoenvironment description	Lithofacies	Horizons marking depositional change
<i>Depositional Sequence 6 (MIS 21-20)</i>	<i>Transgressive</i>	Facies A1 was deposited in gradually deepening inner-to-mid shelf environments under episodic sedimentation and hypoxic conditions.	Facies A1 is a fining-upward clay/silt unit with sparse macrofaunal fossils, interspersed with upwardly thinning sand layers barren of fossils.	<b>-22.5 m:</b> <i>Transgressive surface</i> (=maximum regressive surface) at the D-A1 facies boundary, marked by a thin shell layer.
		Facies A2 was deposited in deeper water settings (outer shelf) with variable oxygenation of sediments and reduced sedimentation rates.	Facies A2 is composed of homogeneous clay-rich deposits with fossil content increasing upward and punctuated by small clumps of oysters.	<b>-21.0 m:</b> A1-A2 facies boundary, transitional lithology and fossil assemblages.
		Facies B is interpreted as firmgrounds mantled by concentration of gregarious ostreids and formed under sediment-starved conditions in an outer shelf-slope setting.	Facies A2 grades into unit B, which is a fossil-rich clay-silt unit	<b>-19.25 m:</b> A2-B facies boundary, transitional lithology and shift in pollen assemblages. Unit B marks the turnaround between transgressive and regressive stacking patterns of facies = <i>Maximum Flooding Zone</i>
	<i>Regressive</i>	Facies C1 records a transition from outer to a mid-shelf setting with increased climate-driven fluvial transport. In the upper part of the unit, several proxies suggest that the shallowing from outer shelf to mid-shelf settings during deposition of upper portion facies C1 was more stepwise than continuous.	Facies C1 begins as a massive muddy-silt package rich in bryozoans that decrease in abundance rapidly before changing to amalgamated silty beds with sparse macrofossils and an ostracod assemblage preferring sandy substrates.	<b>-18.5 m:</b> B-C1 facies boundary, increase in sedimentation rates  <b>-16.0 m:</b> C1-C2 facies boundary, marked by a thin (10 cm) layer of black <i>Chondrites</i> -rich sediment indicative of a short-lived period of low oxygen bottom waters. <b>-15.0 m:</b> C2-C3 facies boundary increase to relatively high sedimentation rates. <b>-13.25 m:</b> Midpoint of facies C3, distinct serpulid horizons and rapid decline in alpine forest pollen. <b>-11.50 m:</b> C3-D facies boundary. In Scarponi et al., 2014 this surface was tentatively interpreted as the RSME (regressive surface of marine erosion). <b>-10.25 m:</b> Lower facies D, sudden minimum in total ostracods, after which a reduced abundance of ostracods preferring sandy substrates return before declining again. <b>-8.75 m:</b> Mid facies D, lithology changes, peak abundance of the steppe pollen assemblage. <b>-6.0 m:</b> Upper facies D, sedimentation rate rapidly increases to its peak within the section, oak pollen becomes more abundant. <b>-17.0 m:</b> Internal subdivisions within facies C1, changes in lithology, fossil assemblages and the pollen recordD
		Facies C2 is deposited in mid-shelf settings with vegetated cover at the bottom.	Facies C2 is a clay-rich unit made of couplets of alternating fossil-rich coarse silts and dark poorly fossiliferous layers of soft muds.	
		Facies C3 is initially a low energy mid-shelf environment characterized by frequent mud blanketing, which shallows upward to a prodelta setting.	Facies C3 is a silt-rich deposit with increasing vegetal debris upwards.	
		Facies D is distal to intermediate delta front with background sedimentation of settling mud punctuated by thin sandy strata indicating high energy events such as river floods and/or storm events that increase upward.	The lower facies D is very similar to the top of C3, with intercalated silt and sand layers with organic-rich laminae containing abundant plant debris and few macrofossils. The upper half of facies D becomes a coarser unit lacking fossils.	

Increased  
regional  
subsidence

(continued on next page)

Table 1 (continued)

	SSP	Paleoenvironment description	Lithofacies	Horizons marking depositional change
<b>Depositional sequence 7 (MIS 19-18)</b>	Transgressive	Facies E fossil assemblage is indicative of mixed sand/mud substrates subject to the influence of riverine waters (mid-shelf settings). E is interpreted to represent prodelta deposits during a short standstill in the transgression (Scarponi et al., 2014)	Facies E is a silty to fine sand unit with a macrofaunal assemblage dominated <i>Turritella tricarinata</i> .	<b>-4.5 m:</b> D-E facies boundary, marked by a layer of disarticulated and oriented shell deposits indicates the <i>Transgressive surface</i> .
		Lower facies A1 fossil assemblage is characteristic of hypoxia and/or high (but rapidly decreasing) sedimentation rates developed within a mid-shelf setting	The lower half of facies A1 has a very similar lithology to facies E with abundant plant debris but scarce macrofossil content. Upper facies A1 is a fining-upward clay/silt unit with sparse macrofaunal fossils.	<b>-2.5 m:</b> E-A1 facies boundary, reported as a flooding surface (Capraro et al., 2017), abrupt change from dominant <i>T. tricarinata</i> species to dominant vegetal debris.
		Upper facies A1 was deposited in rapidly deepening mid to outer shelf environments.		<b>-1.5 m:</b> Midpoint of facies A1, sedimentation rates suddenly drop, mixed oak pollen assemblages become dominant, ostracods preferring muddy substrates return in the record.
	Regressive	Facies A2 indicates deeper water environments (outer shelf) with increased oxygenation at the bottom.	Facies A2 is composed of homogeneous clay-rich deposits punctuated upward by isolated oysters.	<b>0 m:</b> Pitagora ash layer (used here as our datum), at or very near the A1-A2 facies boundary, scarcity of ostracod fossils.D
		Facies B is interpreted to be firmgrounds formed in sediment-starved conditions in an outer shelf-slope setting.	Lithology of facies A2 grades into unit B, which is a fossil-rich clay-silt unit (clumps of gregarious ostreids).	<b>2.3 m:</b> A2-B transitional, increase in concentration of biogenic material and peak in pollen assemblages of deciduous forests. Unit B marks the turnaround between retrogradational and progradational stratal stacking patterns ( <i>Maximum Flooding Zone</i> ).
		Facies C1 records a gradual shallowing from outer to mid-shelf settings.	Facies C1 is a massive fossil-rich clay and silt strata, overall slightly coarsening upward.	<b>3.0 m:</b> B-C1 facies boundary, increase in sedimentation rates
		Facies C2 remains a mid-shelf setting, shallowing upward.	Facies C2 is a thick package of alternating silts and sands enriched in bryozoans with sparse molluscs.	<b>4.3 m:</b> Mid-C1, transition to thin graded sandy layers, peak in alpine forest pollen, <b>5.3 m:</b> C1-C2 facies boundary, marked by a <i>Chondrites</i> -rich black layer as at -16.0 m, but lithology and fossils assemblages are different.
		Facies C3 suggest a shallowing in mid-to-inner-shelf settings.	Facies C3 is a clay-rich unit with sparse bryozoans and molluscs characterized by abrupt shifts in water depths, that grades into a laminated silt/clay layers (upper C3) that is rich in serpulids and vegetal debris.	<b>7.3 m:</b> C2-C3 facies boundary, shift to massive silt unit with loose mollusks and bryozoans.
				<b>9.3 m:</b> Mid facies C3, greater abundance of serpulids and vegetal debris, decline in ostracods preferring sandy substrates, indicating unstable mixed substrates with higher sedimentation rates and high turbidity. <b>11.0 m:</b> Upper facies C3, peak in sandy substrates followed by a decline to zero ostracods at the top of the section, decline in forest pollen (although no increase in steppe pollen).

carbon isotopic composition were measured using an Elemental Analyzer (ECS 4010 - Costech) coupled to an isotope ratio mass spectrometer (Delta V + Thermo Scientific EA-IRMS) at Washington University in St. Louis (MO, USA). Carbon isotope ratios are reported in standard delta notation as permil deviation from the Pee Dee Belemnite (PDB) standard. Isotopic measurements were calibrated against international standards USGS 24 (graphite;  $-16.1‰ \pm 0.07$ ; Coplen et al., 2006), IAEA CH-6 (sucrose;  $-10.45‰ \pm 0.03$ ; Coplen et al., 2006), and IAEA CH-3 (cellulose;  $-24.72‰ \pm 0.04$ ; Coplen et al., 2006). Measurement uncertainty was monitored throughout the analyses using check standards: USGS40 (L-glutamic acid;  $-26.4‰ \pm 0.04$ ) and USGS41 (L-glutamic acid;  $37.6‰ \pm 0.05$ ). Precision was determined to be  $\pm 0.21‰$  based on repeat analyses of check standards. Accuracy was determined to be  $\pm 0.42‰$  based on the difference between the ob-

served and known values of the check standards and the long-term standard deviations of these check standards (after the methods in Szpak et al., 2017). Total organic carbon (TOC) concentrations and total nitrogen (TN) were measured using the Thermal Conductivity Detector (TCD) of the Costech ECS and calibrated with an acetanilide standard (Costech 031040; %C 71.1%; %N 10.4%). Accuracy and relative standard deviation ( $1\sigma$ ) based on standards for %TOC was  $0.05\% \pm 0.03\%$  and for %N was  $0.15\% \pm 0.05\%$ . Precision of %TOC based on sample replicates was determined to be 0.04% (after the methods in Szpak et al., 2017).



## 4. Results

### 4.1. Reduced sulfur record

The abundance of pyrite is relatively low ( $<0.2$  wt% in the bulk sediment) with no obvious trends between glacial and interglacial intervals (Table S1). The bulk isotopic composition of pyrite ( $\delta^{34}\text{S}_{\text{pyr}}$ ), however, increases (i.e., is more enriched in  $^{34}\text{S}$ ) in regressive deposits accumulated during glacials, and decreases toward a minimum in both condensed intervals that mark the turnaround between the transgressive and the regressive systems tracts (TST and RST, respectively; Figs. 2, 3). The minimum bulk  $\delta^{34}\text{S}_{\text{pyr}}$  has a comparable value ( $\sim -40\text{‰}$ ) in both depositional sequences and occurs predominantly within and just below the richly fossiliferous facies B as defined by Carraro et al. (2017; see also Table 1). Superimposed on this gradual oscillatory nature of the  $\delta^{34}\text{S}_{\text{pyr}}$  record, there are distinct multi-point fluctuations that span  $\sim 20\text{‰}$  over 2–3 m intervals, mainly located within the RST of sequences 6 and 7 (i.e., facies C2 through D; Figs. 2, 3). The only such fluctuation that occurs during a transgressive period is capped by the Pitagora Ash deposit (at 0 m). At two intervals (at  $-18$  m and  $+7$  m, respectively), rapid and very large variations ( $>40\text{‰}$ ) in  $\delta^{34}\text{S}_{\text{pyr}}$  occur in the lower regressive units of both sequences and include ‘super-heavy’ (Ries et al., 2009) outlier  $\delta^{34}\text{S}_{\text{pyr}}$  values of  $+54 (\pm 0.02)\text{‰}$  and up to  $+104\text{‰}$  (Fig. 3). The latter, extremely  $^{34}\text{S}$ -enriched outlier (at 6.5 m) was extracted twice and analyzed three times with a standard deviation of  $1.7\text{‰}$  between extractions.

### 4.2. Organic carbon record

The isotopic composition of bulk organic matter ( $\delta^{13}\text{C}_{\text{org}}$ ) in VdM sediments in general is more  $^{13}\text{C}$ -enriched during transgressive deposits (sequence 6 TST mean:  $-25.4 \pm 0.3\text{‰}$  ( $1\sigma$ ); sequence 7 TST mean:  $-25.7 \pm 0.7\text{‰}$  ( $1\sigma$ )) and more  $^{13}\text{C}$ -depleted during regressive deposits (sequence 6 RST mean:  $-26.3 \pm 0.6\text{‰}$ ; sequence 7 RST mean:  $-26.0 \pm 0.4\text{‰}$ ) (Fig. 3). In addition, there is a noticeable negative excursion of  $\delta^{13}\text{C}_{\text{org}}$  ( $\sim 2\text{‰}$ ), over a 1 m interval below the Pitagora ash deposit at  $-1.5$  m (Fig. 3). The relative abundance of TOC in the sam-

ples, in general, is relatively low ( $<0.4$  wt%) during interglacial periods (MIS 21, 19) and higher ( $0.5$ – $1$  wt%) during glacial periods (MIS 20, 18) (Fig. 3). Carbonate content is modest throughout the whole section, with slightly higher abundance in transgressive deposits (mean:  $\sim 29\%$ , minimum:  $19\%$ ) than in regressive units (mean:  $\sim 25\%$ , minimum:  $9\%$ ) (Fig. 3). Carbonate abundance shows only a weak correlation with changes in %TOC ( $R^2 = 0.25$ ,  $p < 0.01$ ; Table S1). The sediments deposited during the middle regressive unit of sequence 6 (facies C3 to early D;  $-15$  to  $-8$  m) have much higher and more variable TOC abundance than those of the following regressive unit (i.e., same facies of sequence 7). The C:N abundance ratio of the TOC in these sediments also tracks glacial-interglacial cycles, with lower values (commonly  $<10$ ) during transgression and values  $>10$  mainly recorded during regression. As with the other proxies, the regressive deposits of sequence 6 are characterized by much higher and more variable C:N ratios than the RST deposits of sequence 7 (Fig. 3). In contrast to  $\delta^{13}\text{C}_{\text{org}}$  values that gradually change throughout the record, the abundance and C:N ratio of organic carbon show abrupt changes at lithologic boundaries in this record. For example, during the MIS 21–20 transition an initial increase in %TOC and increase in C:N ratio begins in the upper portion of facies C1, with an abrupt increase in both at the boundary between facies C2 and C3 ( $-15.0$  m) (Fig. 3). The C:N ratio abruptly decreases at the lithology change midway through facies D of sequence 6 (Fig. 3). Shortly after this ( $-7.5$  m) TOC also decreases back to pre-C1 levels. The TOC and C:N ratio increase again during the C2–C3 boundary ( $7.3$  m; RST of sequence 7), although not as dramatically as during the previous forced regression (Fig. 3), and gradually decrease in the upper portion of facies C3 ( $\sim 11.0$  m). Only the lower-middle part of the RST of sequence 7 (i.e., MIS 18) was sampled here, precluding a complete comparison with the regressive unit accumulated during T-R sequence 6 (i.e., MIS 20).

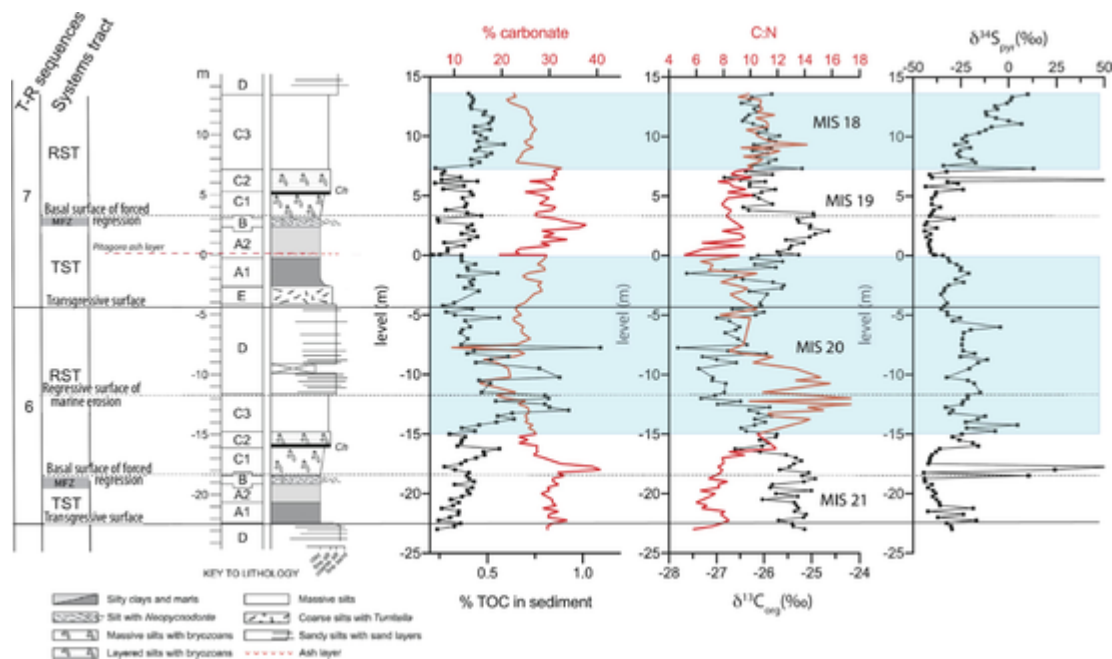


**Fig. 3.** Bulk geochemical proxy records of % carbonate, % organic carbon (TOC), ratio of %TOC to % total nitrogen (C:N) and isotopic composition of organic carbon ( $\delta^{13}\text{C}_{\text{org}}$ ) and pyrite sulfur ( $\delta^{34}\text{S}_{\text{pyr}}$ ) produced in this study. All data, including pyrite % abundance (not shown here), is tabulated in Table S1. Blue highlighted regions mark the glacial stages MIS 18 and 20 reported in Azzarone et al. (2018). (For interpretation of the references to colour in this figure legend, the reader is referred to the web version of this article.)

## 5. Discussion

### 5.1. Sequence stratigraphy at Valle di Manche

The compilation of numerous existing environmental proxy records with our geochemical data from the Valle di Manche section are used here to constrain sediment source and changes in both the sediment accumulation rate and accommodation space in the context of glacial-interglacial cycles to aid the interpretation of our  $\delta^{34}\text{S}_{\text{pyr}}$  record. The TST in both T-R sequences (facies A1-B in Figs. 2, 3) represents a genetically related tract of facies, forming a retrogradational stacking pattern transitioning from inner to outer shelf environments (Rossi et al., 2018 and references therein). Facies B records the last phase of increasing relative sea level based on the benthic  $\delta^{18}\text{O}$  record (Capraro et al., 2015, 2017; Scarponi et al., 2014), leading to sediment starvation, and thus represents the turnaround between retrogradational and progradational stratal stacking patterns in both sequences (Massari et al., 2002, 2007). However, there are slight differences between the sequences as well. For example, the deposits of facies E and lower A1 during the early transgression of the T-R sequence 7 are inferred to represent episodic sedimentation pulses in relatively shallow environments connected to a short stand-still in relative sea-level rise, which are not recognized in sequence 6 (Rossi et al., 2018 and references therein). In addition, the thickness of sequence 7 is expanded due to the increase in local tectonic subsidence rates after MIS 21 (Massari et al., 2007 and references therein), while the stratigraphic record of the lower part of sequence 6 (MIS 21 interglacial) is largely incomplete due to extremely low net sedimentation rates (Fig. 2; Capraro et al., 2015, 2017).

The lower regressive deposits (i.e., accumulated during rapid decrease in sea level) in both sequences record a subsequent shift from outer shelf to inner shelf environments during facies C1 through C3 (Fig. 2). However, beyond this general similarity, significant differences in climate and vegetation cover (Capraro et al., 2005), resulted in different sediment accumulation rates and delivery of organic material to the shelf. For example, the increase in both abundance and terrestrial fraction of organic matter from facies C2 to C3 during sequence 6 (Fig. 3) are consistent with increasing fluvial discharge resulting from a transition through a brief period of cold, wet climate to predominantly cold arid conditions (upper facies C3, sequence 6; Fig. 2). This climate transition led to deforestation and mass wasting, significantly higher terrestrial input, and very high sediment accumulation rates (Massari et al., 2007), setting the mode for rapid progradation of inner shelf deposits during the glacial interval of sequence 6 (facies C3-D in Fig. 2). In contrast, the pollen record in the lower RST of sequence 7 (facies C1-C3) indicates prolonged stability of the alpine forest ecosystem, suggesting less overall terrestrial sediment delivery to the shelf relative to sequence 6 (Figs. 2, 3). At this same time, synclinal growth to the north-west (see Geologic Setting; Massari et al., 2002), as recorded within the proximal sector of the SM sub-basin (Massari et al., 2007), led to expanded stratigraphy especially in the RST of sequence 7 at VdM. Such tectonic conditions may have increased (particularly with respect to the previous C3 unit) the frequency of massive accumulation pulses, delivered by higher gradient and short-headed streams, producing important but cryptic erosional surfaces that may have caused the underestimation of sediment accumulation rates as calculated here.

### 5.2. Interpretation of the sulfur isotope record in pyrite

#### 5.2.1. Sequence stratigraphy and patterns in $\delta^{34}\text{S}_{\text{pyr}}$

The general trends of more  $^{34}\text{S}$ -depleted  $\delta^{34}\text{S}_{\text{pyr}}$  during interglacial periods and more  $^{34}\text{S}$ -enriched  $\delta^{34}\text{S}_{\text{pyr}}$  during glacial periods are similar to observations made in other studies of more recent glacial-interglacial cycles from the Mediterranean (Pasquier et al., 2017). It was suggested that the differences in  $\delta^{34}\text{S}_{\text{pyr}}$  between sediments deposited during the glacials and interglacials were ultimately related to differences in the

sedimentation regime that would influence both delivery and burial rates of organic carbon and the rates at which sediments become isolated from the overlying water column (Pasquier et al., 2017; Liu et al., 2019). In this study, the geochemical proxy records can be interpreted in the context of existing paleoenvironmental and sequence stratigraphic frameworks.

The  $\delta^{34}\text{S}_{\text{pyr}}$  values characterizing TST units of sequences 6 and 7 tend to be more consistent and have less stratigraphic scatter (i.e., ‘noise’, defined as single sample anomalies) with mean and  $1\sigma$  values of  $-34.9\text{‰} \pm 8.2\text{‰}$  and  $-35.1\text{‰} \pm 6.9\text{‰}$ , respectively. In contrast, RST units of sequences 6 and 7 are both characterized by more  $^{34}\text{S}$ -enriched values with more scatter (mean and  $1\sigma$  values of  $-21.5\text{‰} \pm 17.2\text{‰}$  and  $-18.4\text{‰} \pm 24.8\text{‰}$ , respectively; Fig. 3). In addition, in the RST units, the variability in  $\delta^{34}\text{S}_{\text{pyr}}$  often manifests as meter-scale excursions (i.e., multiple samples describing a peak in  $\delta^{34}\text{S}_{\text{pyr}}$  prior to returning to the original  $^{34}\text{S}$ -depleted baseline value). The distribution of  $\delta^{34}\text{S}_{\text{pyr}}$  in transgressive deposits has a peak in frequency around  $-40\text{‰}$ , and no values above  $-15\text{‰}$  (Fig. 4a) with the lowest values in the uppermost TST (Fig. 3). The regressive units of both sequences are also similar, with a distribution that tails up to  $+25\text{‰}$  and includes outliers, with values becoming more  $^{34}\text{S}$ -enriched as time progresses (arrow in Fig. 4b). The lower RST units of both cycles (i.e.,  $-18.5$  to  $-12$  m and  $3$  to  $10.8$  m) retain a significant population ( $\sim 85\%$ ) with  $\delta^{34}\text{S}_{\text{pyr}}$  below  $-10\text{‰}$  (Fig. 4b, solid black and red bars). However, the distributions of  $\delta^{34}\text{S}_{\text{pyr}}$  during the two upper regressive units are very distinct, with a peak frequency of  $\sim -20\text{‰}$  in the sequence 6 and  $\sim 0\text{‰}$  in sequence 7 (Fig. 4b, grey and open bars).

When deposition occurs in deeper water (e.g., mid- to outer shelf deposits), the relative impact of sea-level change is diminished and such deposits are more conducive to recording a less scattered  $\delta^{34}\text{S}_{\text{pyr}}$  stratigraphic signature that is diagnostic of more open-system conditions. This difference is thought to reflect changes in the relative importance of diffusional and burial sources of porewater sulfate during deposition (Claypool, 2004). Fine-grained offshore sediments are usually deposited more slowly in relatively quiescent environments, where diffusion outpaces burial rates. In such depositional environments, effective communication with the overlying water column is expected to lead to a slow decrease with depth in the concentration of porewater sulfate such that the fraction of sulfate remaining ( $f_{\text{SO}_4}$  remaining) is high (Fig. 5). This results in a correspondingly slow increase in the  $\delta^{34}\text{S}$  of pore-water sulfide produced by MSR and minimal  $^{34}\text{S}$ -enrichment in the resulting pyrites formed in these settings. Therefore, the  $\delta^{34}\text{S}_{\text{pyr}}$  values in these deeper water deposits should more faithfully reflect seawater  $\delta^{34}\text{S}_{\text{SO}_4}$  offset by microbial fractionation.

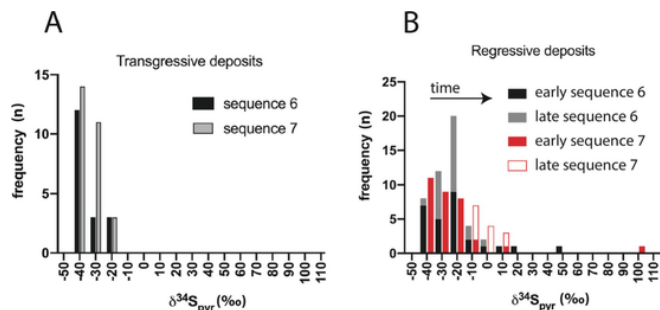


**Fig. 4.** Frequency of bulk  $\delta^{34}\text{S}_{\text{pyr}}$  values during each transgression (A), and regression (B). The general change in values as time progresses are indicated with an arrow (see Fig. 3). The lower regressive deposits in both sequences (black and red shaded bars) capture a wide range in  $\delta^{34}\text{S}_{\text{pyr}}$  with similar distributions, while the upper regressive deposits (grey and open bars) are typically more  $^{34}\text{S}$ -enriched and show clear differences between sequences. (For interpretation of the references to colour in this figure legend, the reader is referred to the web version of this article.)

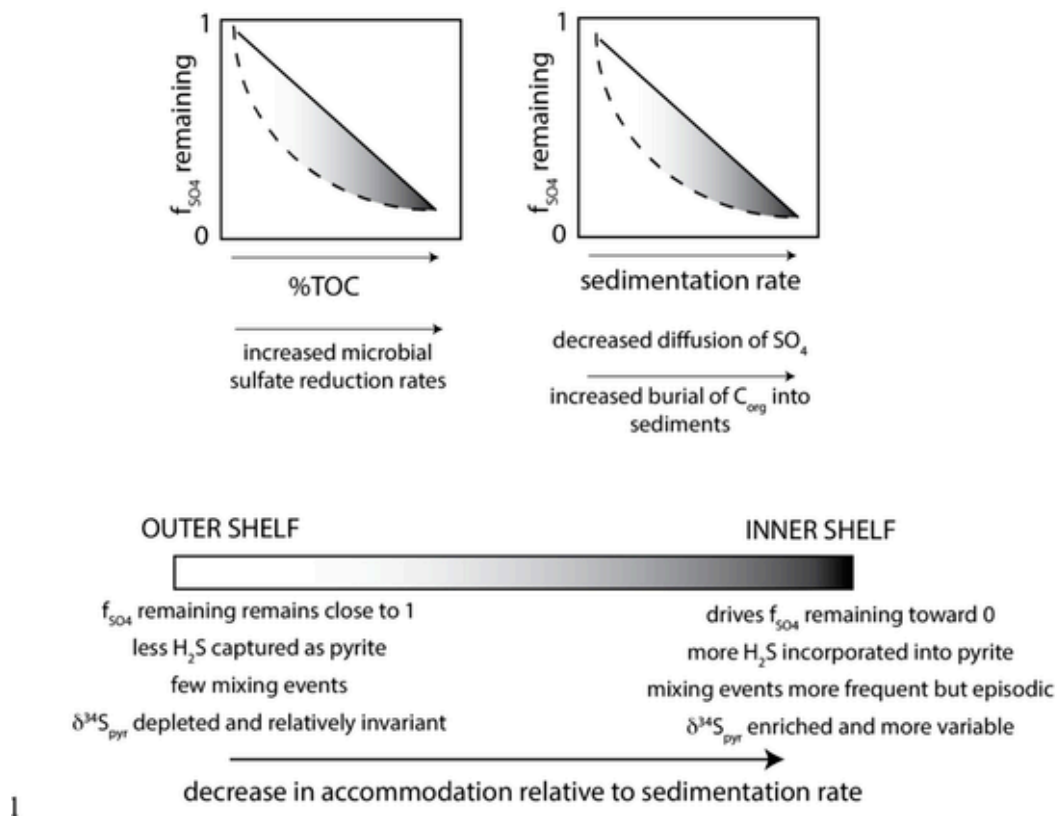


**Fig. 5.** Schematic illustrating hypothetical changes in the fraction of sulfate remaining ( $f_{SO_4}$ ) as a function of key environmental parameters described in the text. The associations may be linear (solid lines) or non-linear (dashed lines) but are expected to progress as deposition shifts from the outer to inner shelf environments as the relative sea-level rise is higher than the sediment accumulation rate.

However, sediments deposited in shallower environments are typically characterized by more rapid, less steady sediment accumulation rates and high rates of organic matter and reactive iron delivery. In these proximal settings, the geochemical signal of sea-level change becomes overprinted by repeated disturbances inherent to higher energy environmental settings, creating more spread in the absolute  $\delta^{34}S_{pyr}$  values (e.g.,  $1\sigma$  values for RST vs. TST; Fig. 4b). In addition, in such nearshore-inner shelf settings, smaller shifts in relative sea level will have a greater impact on the parameters defining depositional environments, leading to more variability from one glacial cycle to the next (Fig. 4b).

#### 5.2.2. Connecting the environment of deposition to microbial sulfur cycling and pyrite formation

The sedimentation style of the regressive deposits of the VdM section (best exposed in sequence 7) indicates that sediments were delivered by short-headed streams draining the Sila massif (Massari et al., 2007). Due to the close proximity of the terrestrial source and limited space for sediment storage in the catchment, major changes in sediment source and supply caused by climate variations are transferred from source to sink with little apparent attenuation (Massari et al., 2007). Therefore, the total organic carbon (%TOC) and the ratio of total organic carbon to total nitrogen (C:N) can be used to indicate significant changes in the supply and source, respectively, of sediment reaching the seafloor. Lower C:N values ( $<10$ ) indicate a dominantly marine source (planktonic or bacterial; Hedges et al., 1986; Hedges et al., 1997), while higher values ( $>20$ ) indicate greater incorporation of terrestrial organic matter due to the abundance of nitrogen-free compounds in plant materials (e.g., tannins, resins, cuticular waxes, lignin, hemicelluloses; Hedges et al., 1997). Degradation of organic matter within sediments will impact the C:N ratio, with plant matter preferentially gaining nitrogen and marine plankton losing nitrogen during mi-

crobial decay, resulting in converging ratios of both endmember sources (Hedges and Oades, 1997). The C:N values in this study range from 6 to  $\sim 18$ , indicating a mixed marine and terrestrial source of organic matter throughout the section with significant increases in the terrestrial component particularly during MIS 20 (Fig. 3). The isotopic composition of bulk organic carbon ( $\delta^{13}C_{org}$ ) can also indicate sediment source. Most terrestrial plants use the Calvin-Benson cycle (C3) for metabolism that produces biomass  $\delta^{13}C_{org}$  of  $-28$  to  $-25\text{‰}$ , while C4 plants such as grasses produce biomass  $\delta^{13}C_{org}$  near  $-12\text{‰}$  (Hedges et al., 1997; McMillan et al., 1980). Marine plankton biomass has  $\delta^{13}C_{org}$  between  $-22$  and  $-19\text{‰}$  (Fry and Sherr, 1989), although the ranges vary with species,  $CO_2$  abundance, growth rate, and light/nutrient availability (Hedges et al., 1997). The  $\delta^{13}C_{org}$  values in this study range from  $-27.5$  to  $-25\text{‰}$ , suggesting that terrestrial biomass is the dominant source of organic material supplied to these shelf environments (Fig. 3). However, the  $\delta^{13}C_{org}$  can change up to  $5$ – $10\text{‰}$  during preferential degradation of different components of biomass, making nuances in the bulk  $\delta^{13}C_{org}$  difficult to interpret (Hedges et al., 1997).

Throughout the VdM section, we also observe a good correlation between %TOC and the C:N ratio ( $r^2 = 0.62$ ,  $p < 0.01$ ; Table S1), which suggests greater burial of organic matter coincides with greater preservation of terrestrial sources that would both have a direct impact on the rates of sulfate reduction in sediments (as reviewed in Fike et al., 2015). Thus, in proximal settings, diffusive timescales are long relative to the rate of burial and microbial sulfate reduction rates may increase due to higher organic carbon loading. In such settings, porewater sulfate becomes effectively isolated from the overlying water-column sulfate reservoir and MSR drives the  $f_{SO_4}$  remaining toward zero at a relatively shallow depth within the sediment (Fig. 5). A rapid MSR-driven decrease in the concentration of porewater sulfate and the associated isotopic discrimination results in down-sediment enrichment in  $^{34}S$  of the residual sulfate and the instantaneously produced sulfide (Fig. 5). Fur-

thermore, in cases of enhanced delivery of reactive iron, an increase in the effective sequestration of MSR-produced sulfide in iron sulfide minerals can occur. Such effects can explain the large and systematic  $\delta^{34}\text{S}_{\text{pyr}}$  variations at the temporal scale of glacial-interglacial cycles (i.e., 100 kyr) observed in (Pasquier et al., 2017) that were correlated to sea-level-driven changes in sedimentation rate.

Based on the compilation of paleoenvironmental proxies discussed above, the stratigraphy of the VdM section is presented with the sulfur isotope composition of bulk pyrite ( $\delta^{34}\text{S}_{\text{pyr}}$ ) reported in this study (Fig. 6). We can use our geochemical proxies to test whether the conceptual framework and associations described in Fig. 5 could explain the observed  $\delta^{34}\text{S}_{\text{pyr}}$  record, assuming that (1) changes in eustatic sea level can be estimated by the benthic foram  $\delta^{18}\text{O}_{\text{U. peregrina}}$  (sea level) normalized to the maximum value, and (2) these changes are the sole driver for the creation/consumption of accommodation space (labeled sea level). The %TOC normalized to the maximum value, sedimentation rate, and  $\delta^{18}\text{O}_{\text{U. peregrina}}$  (sea level) normalized to the maximum value again highlight the asynchronous shifts in organic carbon, sedimentation rate and eustatic sea-level change (Fig. 6). In principle, higher %TOC (modulated to some extent by the terrestrial vs. marine source) stimulates microbial sulfate reduction (MSR) and leads to more  $^{34}\text{S}$ -enriched  $\delta^{34}\text{S}_{\text{pyr}}$ , pending Fe availability, such that the  $\delta^{34}\text{S}_{\text{pyr}}$  should track with TOC (Fig. 6). However, the sedimentation rate also plays an important role, such that greater enrichment of

$^{34}\text{S}$  in pyrite occurs when sediment accumulation rate exceeds the rate of sea-level rise (causing sulfate diffusion rates to decrease) and thus will amplify the effects of MSR during lowstands and dampen those effects during transgressions (Fig. 6). Combining these 3 factors in a simplistic parameterization that accounts only for eustatic sea-level changes:

$$\text{Enrichment in } \delta^{34}\text{S}_{\text{pyr}} \sim \frac{(\% \text{TOC} \times \text{sedimentation rate})}{\text{sea level} * } \quad (1)$$

results in a record that reproduces the general trends in the  $\delta^{34}\text{S}_{\text{pyr}}$  record surprisingly well, given the low-resolution data available for sedimentation rates (Fig. 6).

It is apparent that when the rate of sea-level\* rise exceeds the sediment accumulation rate, this simple conceptual model predicts the observed trend of relatively invariant and  $^{34}\text{S}$ -depleted  $\delta^{34}\text{S}_{\text{pyr}}$  values. However, during progradational phases when accommodation space is low, either due to increasing sediment accumulation rates (e.g., -23 to -21 m and -15 to -3 m), or due to relative sea-level fall (e.g., +5 to +10 m), or a combination of changes in both (e.g., -3 to 0 m), the  $\delta^{34}\text{S}_{\text{pyr}}$  exhibits much greater scatter. Additionally, the  $\delta^{34}\text{S}_{\text{pyr}}$  record appears more sensitive to in-situ sediment conditions controlled by local changes in the environment, suggesting other forcing factors are involved that are not represented in this simple parameterization (Fig. 6).

### 5.2.3. Effects of climate, subsidence, and erosion: Local processes overprinting the eustatic signal

In addition to these general forcing factors, the  $\delta^{34}\text{S}_{\text{pyr}}$  record appears to capture detail on time scales  $< 10^4$  years that is likely controlled by local forcing factors, such as basin geometry and river influx, as well as changes in hydrodynamics and bottom currents. All these factors can affect geochemical redox gradients (driven by microbial processes such as MSR) and the precipitation of pyrite below the sediment-water interface. We highlight examples where these local factors can result in divergent patterns in  $\delta^{34}\text{S}_{\text{pyr}}$  (relative to those predicted by our model from eustatic changes). This divergence results from, and is amplified by, subtle differences in environmental conditions, despite the apparent repetition of environments represented by the stratal stacking patterns in sequence 6 and 7.

In contrast to the relatively stable signal recorded in transgressive deposits of both sequences, the  $\delta^{34}\text{S}_{\text{pyr}}$  values of the regressive unit of sequence 6 exhibit several multiple-point excursions that are  $^{34}\text{S}$ -enriched relative to a minimum value of  $\sim -32\text{‰}$  (Fig. 3; vertical dashed red line in Fig. 6). At certain facies boundaries and wherever a substantial change in lithology, fossil assemblages or geochemical param-

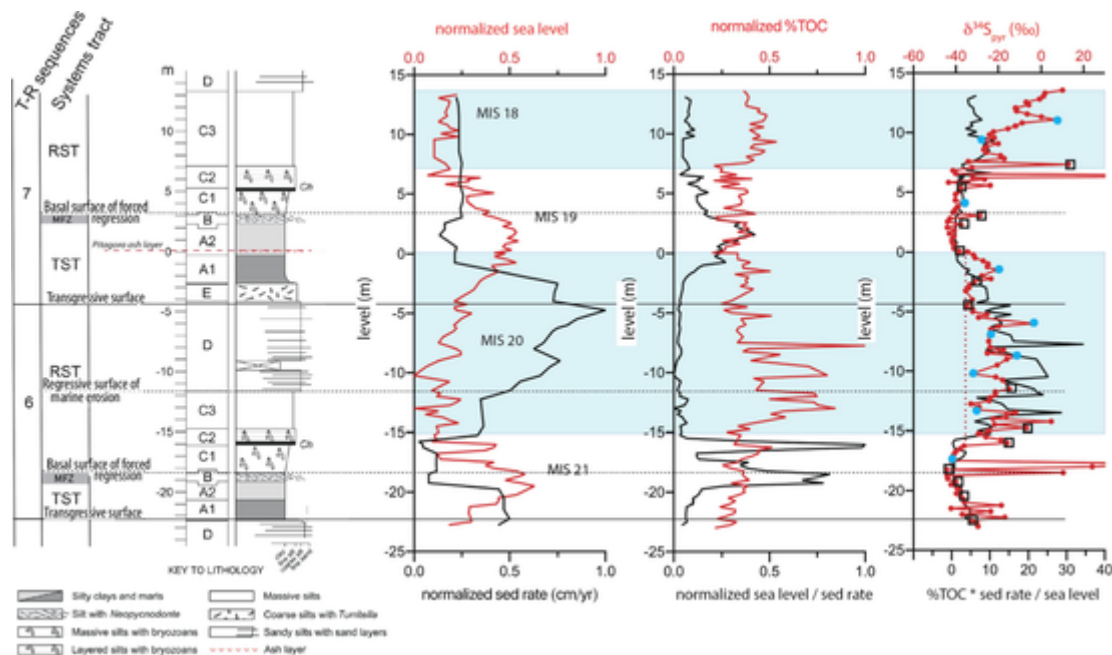


**Fig. 6.** Key environmental parameters (sedimentation rate, %TOC, and eustatic sea level approximated by  $\delta^{18}\text{O}_{\text{U. peregrina}}$ ) are shown normalized to their maximum values in the section. An approximation of accommodation space is shown as the ratio of sea level to sedimentation rate (middle panel, black). Our simple parameterization is shown on the right in black compared to the bulk  $\delta^{34}\text{S}_{\text{pyr}}$  values in red. Dashed vertical red line indicates the minimum baseline  $\delta^{34}\text{S}_{\text{pyr}}$  during the RST of sequence 6. The  $\delta^{34}\text{S}_{\text{pyr}}$  values at facies boundaries are superimposed with open black squares, while those at which one or more environmental parameters (see text) change abruptly are indicated with blue circles. Blue highlighted regions mark the glacial stages MIS 18 and 20. (For interpretation of the references to colour in this figure legend, the reader is referred to the web version of this article.)



ters (e.g., %TOC or C:N ratio) simultaneously occurs within facies, we note a shift in the  $\delta^{34}\text{S}_{\text{pyr}}$  record (Fig. 6). However, there is no robust association between specific lithologies or %TOC and specific  $\delta^{34}\text{S}_{\text{pyr}}$  values throughout the section. Most excursions occur within the RST deposits (facies C2-D, mid-shelf to delta front) characterized by conditions of seafloor instability associated with sediment flows and numerous erosional surfaces (Table 1). Under these conditions, after a sediment flow buries a given interval the  $\delta^{34}\text{S}_{\text{pyr}}$  might appear as a more gradual excursion due to increased burial of organic matter and isolation of porewaters. During periods between sediment flows when sedimentation rate drops, the  $\delta^{34}\text{S}_{\text{pyr}}$  in the overlying sediments might be expected to suddenly decrease. We suggest, therefore, that the isotopic maxima and minima occur at minor erosional contacts associated with relatively high-energy settings that our simple model cannot parameterize. The  $\delta^{34}\text{S}_{\text{pyr}}$  record instead appears to reflect non-steady state behavior in the sedimentary system.

In two portions of sequences 6 and 7, corresponding to the onset of relative sea level fall, extremely  $^{34}\text{S}$ -enriched outliers are preserved (i.e.,  $\delta^{34}\text{S}_{\text{pyr}} = +55\text{‰}$  at  $-18\text{ m}$ , and  $\delta^{34}\text{S}_{\text{pyr}} = +104\text{‰}$  at  $+6\text{ m}$ ), both closely associated with intermittently  $^{34}\text{S}$ -enriched outliers (i.e., noise) and hosted in richly fossiliferous silty muds (Table 1). Both intervals also are associated with rapid decreases in sea level (Fig. 6) and show evidence of frequent mud blanketing, sometimes decimeters thick (Capraro et al., 2017). It is possible, that such single-point anomalies captured evidence of resuspension and/or erosional events that exhumed and reworked biogenic material before being rapidly covered by fresh mud deposits (Aller et al., 2008; Aller et al., 2010). In modern systems, extremely  $^{34}\text{S}$ -enriched  $\delta^{34}\text{S}_{\text{pyr}}$  values are frequently preserved at, or below the scouring/bioturbation depth due to a priming effect whereby overlying deposition of organic-rich, Fe-rich sediments stimulates further pyrite production from a mixture of pre-existing  $^{34}\text{S}$ -enriched sulfide diffusing upward and renewed sulfate reduction at the interface (as reviewed in Aller, 2014). A prominent example of this, in modern sedimentary environments, is the Guyana mobile mud belt, where frequent remobilization of surface sediment in response to highly energetic currents is responsible for intense cycling of redox conditions, resulting in unusually  $^{34}\text{S}$ -enriched pyrite from  $0\text{‰}$  to  $>30\text{‰}$  (Aller et al., 2010). Other horizons in the VdM section characterized by significantly  $^{34}\text{S}$ -enriched (single-point) noise in the  $\delta^{34}\text{S}_{\text{pyr}}$  record occur during the early transgressive phase of sequence 6 within facies A1, where strictly episodic sedimentation and widespread erosional surfaces were documented (Fig. 6; Capraro et al., 2015, 2017). More detailed sedimentological observations would be needed to better constrain the origin of these anomalies.

In our current parameterization, the estimate of changes in accommodation space is based on the benthic foraminiferal oxygen isotope record (i.e., proxy for global sea level) from this section and cannot account for relative sea-level changes due to local tectonic or other physical processes affecting net sedimentation rates (e.g., avulsion of river channels or delta lobe switching). While the sedimentation rate will be underestimated if erosion occurs, accommodation space will be under-estimated if basin subsidence occurs without a change in eustatic sea level. In either case, the prediction from our parameterization will under-estimate the change in  $\delta^{34}\text{S}_{\text{pyr}}$ . There are two horizons in this section where excursions exist in our data that are not predicted by our parameterization: at the end glacial MIS 18 ( $\sim -5$  to  $0\text{ m}$ ) and the early-mid glacial MIS 20 ( $\sim 10$ – $13\text{ m}$ ). Independent paleoecological proxies (i.e., mollusk and ostracods) suggest short-lived progradation occurred from

$-5$  to  $0\text{ m}$  (deltaic influenced shelf environments) interpreted as the sedimentary response to a sea-level standstill recorded within the TST of sequence 7 (Scarponi et al., 2014; Rossi et al., 2018). However, the benthic foraminiferal  $\delta^{18}\text{O}$  record indicates a steady increase in global sea level over this period, suggesting that regional uplift caused a transient reduction of accommodation space (and change in relative sea level) that is unaccounted for in our current parameterization. At this

same time, an abrupt increase in mixed oak/alpine forest pollen, indicating a tectonically driven shift to higher altitude sediment delivery, is consistent with a significant increase in fluvial discharge during facies A1 (e.g.,  $-3$  to  $0\text{ m}$ ). The combined effects of uplift of the basin and a transient climate-driven increase in sedimentation caused a change in accommodation space that would not be predicted from the eustatic sea-level record.

Likewise, in the second horizon where the calculation underestimates the observed  $\delta^{34}\text{S}_{\text{pyr}}$  (upper facies C3;  $\sim 10$  to  $13\text{ m}$ ), the significantly  $^{34}\text{S}$ -enriched  $\delta^{34}\text{S}_{\text{pyr}}$  values are unexpected given the low calculated net sedimentation rates and relatively low %TOC. However, tectonic uplift in the proximal sector of the basin (Massari et al., 2007) may have increased the frequency of massive accumulation pulses delivered by higher gradient and short-headed streams that more effectively isolated the sediment porewaters from the overlying water column leading to  $^{34}\text{S}$ -enriched porewater sulfide. These pulsed, massive sedimentation events may have also played a major role in producing important but cryptic erosional surfaces that would have caused the underestimation of sediment accumulation rates. Finally, increased iron availability may also have played an important role, allowing continued pyrite precipitation after sudden episodes of sediment burial. The strong positive trend of  $\delta^{34}\text{S}_{\text{pyr}}$  characterizing the uppermost VDM succession hence could be influenced by a combination of repeated episodes of massive sediment accumulation separated by periods of erosion in deltaic-influenced settings (Rossi et al., 2018) that led to an underestimation of the sediment accumulation rate. Thus, it appears that the complex interplay between local tectonics and climate-driven changes in sedimentation rates during sequence 7 at VdM (Massari et al., 2002; Rossi et al., 2018) impacted the bulk  $\delta^{34}\text{S}_{\text{pyr}}$  record, resulting in an overall more  $^{34}\text{S}$ -enriched, and increasing upward  $\delta^{34}\text{S}_{\text{pyr}}$  signal compared to the RST deposits of sequence 6 (Fig. 3).

In the examples discussed above, the divergence in  $\delta^{34}\text{S}_{\text{pyr}}$  patterns from our calculation can be explained by regional processes that create non-steady sedimentation regimes, which are not apparent from the net sedimentation rate. These intervals are the result of inadequate parameterization of the regional interplay between local climate and tectonically generated subsidence, highlighting the necessity for detailed interdisciplinary proxy records that provide independent evidence for regional changes in relative sea level and sedimentation.

## 6. Conclusions

Our findings provide a new perspective on the roles of the local depositional environments and stratal stacking patterns in early diagenetic processes as recorded in sedimentary  $\delta^{34}\text{S}_{\text{pyr}}$ . This study identifies the connections between  $\delta^{34}\text{S}_{\text{pyr}}$  records and depositional environments, highlighting specific settings that warrant more detailed study, including shallow-water deposits and prograding deposits. We predict physical reworking plays a dominant role in shaping the bulk  $\delta^{34}\text{S}_{\text{pyr}}$  composition in the former, while shifting porewater geochemical gradients stimulated by changes in sediment source are important in the latter. Sedimentary  $\delta^{34}\text{S}_{\text{pyr}}$  trends highlight internal detail within stratal stacking patterns and thus may represent a powerful tool for sequence stratigraphic interpretation of siliciclastic sedimentary successions or for re-examination of previously developed sequence stratigraphic frameworks. The evidence presented here reinforces previous observations in modern shelf environments. In shallow depositional environments, rather than recording changes in the global sulfur cycle, the variations in  $\delta^{34}\text{S}_{\text{pyr}}$  reflect sedimentological drivers that vary on timescales much shorter than the residence time of sulfate in seawater. Our study suggests that many of the climatological and geochemical perturbations in deep time that are inferred on the basis of the geologic record of  $\delta^{34}\text{S}_{\text{pyr}}$  in shelf deposits may have been more directly related to changes in the depositional environments than biogeochemical changes in the ocean. Such changes may be triggered globally (e.g., by a

synchronous change in sea level), leading to spatially correlated shifts in  $\delta^{34}\text{S}_{\text{pyr}}$  that do not represent global changes in sulfur cycling or ocean redox. With this in mind, the influence that variations in the depositional environment may have on such geochemical proxy records should be re-examined.

### Declaration of Competing Interest

The authors declare that they have no known competing financial interests or personal relationships that could have appeared to influence the work reported in this paper.

### Acknowledgments

We acknowledge support from McDonnell Center for the Space Sciences, the Environmental Studies Program, and the International Center for Energy, Environment, and Sustainability (InCEES) at Washington University. Thanks to Patrizia Macrì (Istituto Nazionale di Geofisica e Vulcanologia) and Giorgia Dalan (Università di Padova, Italy) for assistance during sampling. We also acknowledge J.W. Huntley (University of Missouri, MO-USA) who introduced us to this fruitful collaboration. We also thank Ben Gill and Guillaume Paris for constructive re-views that improved this paper.

### Appendix A. Supplementary data

Supplementary data to this article can be found online at <https://doi.org/10.1016/j.palaeo.2021.110730>.

### References

Aller, R.C., 2014. Sedimentary diagenesis, depositional environments, and benthic fluxes. In: Holland, Heinrich D., Turekian, Karl K. (Eds.), *Treatise on Geochemistry*, Second edition, Elsevier, pp. 293–334.

Aller, R.C., Mackin, J.E., Cox, Jr., R.T., 1986. Diagenesis of Fe and S in Amazon inner shelf muds: apparent dominance of Fe reduction and implications for the genesis of ironstones. *Cont. Shelf Res.* 6 (1–2), 263–289.

Aller, R.C., Blair, N.E., Brunsell, G.J., 2008. Early diagenetic cycling, incineration, and burial of sedimentary organic carbon in the central Gulf of Papua (Papua New Guinea). *J. Geophys. Res.* 113 (F01S09).

Aller, R.C., Madrid, V., Chistoserdov, A., Aller, J.Y., Heilbrun, C., 2010. Unsteady diagenetic processes and sulfur biogeochemistry in tropical deltaic muds: Implications for oceanic isotope cycles and the sedimentary record. *Geochim. Cosmochim. Acta* 74, 4671–4692.

Azzarone, M., Ferretti, P., Rossi, V., Scarponi, D., Capraro, L., Macrì, P., Huntley, J.W., Faranda, C., 2018. Early-Middle Pleistocene benthic turnover and oxygen isotope stratigraphy from the Central Mediterranean (Valle di Manche, Crotona Basin, Italy): Data and trends. *Data in brief* 17, 1099–1107.

Barone, A., Fabbri, A., Rossi, S., Sartori, R., 1982. Geological structure and evolution of the marine area adjacent to the Calabrian Arc. *Earth Planet. Sci. Lett.* 3, 207–221.

Berner, R.A., 1978. Sulfate reduction and the rate of deposition of marine sediments. *Earth Planet. Sci. Lett.* 37, 492–498.

Berner, R.A., 1980. *Early Diagenesis: A Theoretical Approach* (No. 1). Princeton University Press.

Berner, R.A., 1984. Sedimentary pyrite formation: an update. *Geochim. Cosmochim. Acta* 48 (4), 605–615.

Berner, R.A., Raiswell, R., 1983. Burial of organic carbon and pyrite sulfur in sediments over Phanerozoic time: a new theory. *Geochim. Cosmochim. Acta* 47 (5), 855–862.

Canfield, D.E., 2001. Isotope fractionation by natural populations of sulfate-reducing bacteria. *Geochim. Cosmochim. Acta* 65, 1117–1124.

Canfield, D.E., Raiswell, R., 1992. The reactivity of sedimentary iron minerals toward sulfide. *Am. J. Sci.* 292, 659–683.

Canfield, D.E., Teske, A., 1996. Late Proterozoic rise in atmospheric oxygen concentration inferred from phylogenetic and Sulphur-isotope studies. *Nature* 382 (6587), 127–132.

Canfield, D.E., Raiswell, R., Westrich, J.T., Reaves, C.M., Berner, R.A., 1986. The use of chromium reduction in the analysis of reduced inorganic sulfur in sediments and shales. *Chem. Geol.* 54 (1–2), 149–155.

Capraro, L., Ascoli, A., Backman, J., Bertoldi, R., Channell, J.E.T., Massari, F., Rio, D., 2005. Climatic patterns revealed by pollen and oxygen isotope records across the Matuyama-Brunhes boundary in the Central Mediterranean (southern Italy). *Geol. Soc. Lond., Spec. Publ.* 247 (1), 159–182.

Capraro, L., Consolaro, C., Fornaciari, E., Massari, F., Rio, D., 2006. Chronology of the middle-upper Pliocene succession in the Strongoli area: Constraints on the geological evolution of the Crotona Basin (southern Italy). In: Moratti, G., Chalouan, A. (Eds.), *Tectonics of the Western Mediterranean and North Africa*. Geol. Soc. Lond. Spec. Publ. 262. Geological Society, Bath, UK, pp. 323–333.

Capraro, L., Massari, F., Rio, D., Fornaciari, E., Backman, J., Channell, J.E.T., Macrì, P., Prosser, G., Speranza, F., 2011. Chronology of the lower-middle Pleistocene succession of the south-western part of the Crotona Basin (Calabria, southern Italy). *Quat. Sci. Rev.* 30, 1185e1200.

Capraro, L., Macrì, P., Scarponi, D., Rio, D., 2015. The lower to Middle Pleistocene Valle di Manche section (Calabria, Southern Italy): state of the art and current advances. *Quat. Int.* 383, 36–46.

Capraro, L., Ferretti, P., Macrì, P., Scarponi, D., Tateo, F., Fornaciari, E., Bellini, G., Dalan, G., 2017. The Valle di Manche section (Calabria, Southern Italy): a high resolution record of the Early-Middle Pleistocene transition (MIS 21-MIS 19) in the Central Mediterranean. *Quat. Sci. Rev.* 165, 31–48.

Capraro, L., Tateo, F., Ferretti, P., Fornaciari, E., Macrì, P., Scarponi, D., Preto, N., Xian, F., Kong, X., Xie, X., 2019. A Mediterranean perspective on 10Be, sedimentation and climate around the Matuyama/Brunhes boundary: les liaisons dangereuses? *Quat. Sci. Rev.* 226, 106039.

Claypool, G.E., 2004. Ventilation of marine sediments indicated by depth profiles of pore water sulfate and  $\delta^{34}\text{S}$ . Special Publication, Geochemical Society. 9, 59–65.

Coplen, T.B., Hopple, J.A., Böhlke, J.K., Peiser, H.S., Rieder, S.E., Krouse, H.R., Rosman, K.J.R., Ding, T., Vocke, R.D.J., Révész, K.M., Lamberty, A., Taylor, P., DeBièvre, P., 2002. Compilation of Minimum and Maximum Isotope Ratios of Selected Elements in Naturally Occurring Terrestrial Materials and Reagents, United States Geological Survey. p. 98.

Coplen, T.B., Brand, W.A., Gehre, M., Gröning, M., Meijer, H.A.J., Toman, B., Verhoeven, R.M., 2006. New guidelines for  $\delta^{13}\text{C}$  measurements. *Anal. Chem.* 78, 2439–2441.

Cowie, G.L., Hedges, J.L., 1994. Biochemical indicators of diagenetic alteration in natural organic matter mixtures. *Nature* 369 (6478), 304–307.

Detmers, J., Bruchert, V., Habicht, K.S., Kuever, J., 2001. Diversity of sulfur isotope fractionations by sulfate-reducing prokaryotes. *Appl. Environ. Microbiol.* 67, 888–894.

Fike, D.A., Bradley, A.S., Rose, C.V., 2015. Rethinking the Ancient Sulfur Cycle. *Annu. Rev. Earth Planet. Sci.* 43, 20.1–20.30.

Fry, B., Sherr, E.B., 1989.  $\delta^{13}\text{C}$  measurements as indicators of carbon flow in marine and freshwater ecosystems. In: Rundel, P.W., Ehleringer, J.R., Nagy, K.A. (Eds.), *Stable Isotopes in Ecological Research*. Ecological Studies (Analysis and Synthesis), vol. 68. Springer, New York, pp. 196–229.

Garrels, R.M., Lerman, A., 1984. Coupling of the sedimentary sulfur and carbon cycles; an improved model. *Am. J. Sci.* 284 (9), 986–1007.

Goldhaber, M.B., Kaplan, I.R., 1975. Controls and consequences of sulfate reduction rates in recent marine sediments. *Soil Sci.* 119, 42–55.

Goldhaber, M.B., Kaplan, I.R., 1980. Mechanisms of sulfur incorporation and isotope fractionation during early diagenesis in sediments of the Gulf of California. *Mar. Chem.* 9 (2), 95–143.

Gorjan, P., Kaiho, K., Fike, D.A., Xu, C., 2012. Carbon- and sulfur-isotope geochemistry of the Hirnantian (Late Ordovician) Wangjiawan (Riverside) section, South China: global correlation and environmental event interpretation. *Palaeogeogr. Palaeoclimatol. Palaeoecol.* 337–338, 14–22.

Hammarlund, E.U., Dahl, T.W., Harper, D.A.T., Bond, D.P.G., Nielsen, A.T., Bjerrum, C.J., Schovsbo, N.H., Schönlaub, H.P., Zalasiewicz, J.A., Canfield, D.E., 2012. A sulfidic driver for the end-Ordovician mass extinction. *Earth Planet. Sci. Lett.* 331–332, 128–139.

Hedges, J.L., Oades, J.M., 1997. Comparative organic geochemistries of soils and marine sediments. *Org. Geochem.* 27 (7–8), 319–361.

Hedges, J.L., Clark, W.A., Quay, P.D., Richey, J.E., Devol, A.H., Santos, M., 1986. Compositions and fluxes of particulate organic material in the Amazon River 1. *Limnol. Oceanogr.* 31 (4), 717–738.

Hedges, J.L., Keil, R.G., Benner, R., 1997. What happens to terrestrial organic matter in the ocean? *Org. Geochem.* 27 (5–6), 195–212.

Hedges, J.L., Eglinton, G., Hatcher, P.G., Kirchman, D.L., Arnosti, C., Derenne, S., Evershed, R.P., Kögel-Knabner, I., de Leeuw, J.W., Littke, R., Michaelis, W., 2000. The molecularly-uncharacterized component of nonliving organic matter in natural environments. *Org. Geochem.* 31 (10), 945–958.

Hurtgen, M.T., Arthur, M.A., Halverson, G.P., 2005. Neoproterozoic sulfur isotopes, the evolution of microbial sulfur species, and the burial efficiency of sulfide as sedimentary pyrite. *Geology* 33 (1), 41–44.

Jones, D.S., Fike, D.A., 2013. Dynamic sulfur and carbon cycling through the end-Ordovician extinction revealed by paired sulfate–pyrite  $\delta^{34}\text{S}$ . *Earth Planet. Sci. Lett.* 363, 144–155.

Jørgensen, B.B., 1979. Theoretical-model of the stable sulfur isotope distribution in marine sediments. *Geochim. Cosmochim. Acta* 43 (3), 363–374.

Kaplan, I.R., Rittenberg, S.C., 1964. Microbiological fractionation of Sulphur isotopes. *J. Gen. Microbiol.* 34, 195–212.

Leavitt, W.D., Halevy, I., Bradley, A.S., Johnston, D.T., 2013. Influence of sulfate reduction rates on the Phanerozoic sulfur isotope record. *Proc. Natl. Acad. Sci.* 110, 11244–11249.

Liu, X., Fike, D., Li, A., Dong, J., Xu, F., Zhuang, G., Rendle-Bühning, R., Wan, S., 2019. Pyrite sulfur isotopes constrained by sedimentation rates: evidence from sediments on the East China Sea inner shelf since the late Pleistocene. *Chem. Geol.* 505, 66–75.

Macrì, P., Speranza, F., Capraro, L., 2014. Magnetic fabric of Plio-Pleistocene sediments from the Crotona fore-arc basin: insights on the recent tectonic evolution of the Calabrian Arc (Italy). *J. Geodyn.* 81, 67–79.

Macrì, P., Capraro, L., Ferretti, P., Scarponi, D., 2018. A high-resolution record of the Matuyama-Brunhes transition from the Mediterranean region: the Valle di Manche section (Calabria, Southern Italy). *Phys. Earth Planet. Inter.* 278, 1–15.

Mann, J.L., Vocke, Jr., R.D., Kelly, W.R., 2009. Revised  $\delta^{34}\text{S}$  reference values for IAEA sulfur isotope reference materials S-2 and S-3. *Rapid Commun. Mass Spectrom.* 23, 1116–1124.

Massari, F., Rio, D., Sgavetti, M., Prosser, G., D’Alessandro, A., Ascoli, A., Capraro, L.,

- Fornaciari, E., Tateo, F., 2002. Interplay between tectonics and glacio-eustasy: Pleistocene succession of the Crotona basin, Calabria (southern Italy). *Geol. Soc. Am. Bull.* 114 (10), 1183–1209.
- Massari, F., Capraro, L., Rio, D., 2007. Climatic modulation of timing of systems-tract development with respect to sea-level changes (middle Pleistocene of Crotona, Calabria, southern Italy). *J. Sediment. Res.* 77 (6), 461–468.
- Massari, F., Prosser, G., Capraro, L., Fornaciari, E., Consolaro, C., 2010. A revision of the stratigraphy and geology of the south-western part of the Crotona Basin (South Italy). *Ital. J. Geosci.* 129 (3), 353–384.
- McMillan, C., Parker, P.L., Fry, B., 1980.  $^{13}\text{C}/^{12}\text{C}$  ratios in seagrasses. *Aquat. Bot.* 9, 237–249.
- Mollenhauer, G., Eglinton, T.I., 2007. Diagenetic and sedimentological controls on the composition of organic matter preserved in California Borderland Basin sediments. *Limnol. Oceanogr.* 52 (2), 558–576.
- Pasquier, V., Sansjofre, P., Rabineau, M., Revillon, S., Houghton, J., Fike, D.A., 2017. Pyrite sulfur isotopes reveal glacial–interglacial environmental changes. *PNAS* 114 (23), 5941–5945.
- Peiffer, S., Behrends, T., Hellige, K., Larese-Casanova, P., Wan, M., Pollok, K., 2015. Pyrite formation and mineral transformation pathways upon sulfidation of ferric hydroxides depend on mineral type and sulfide concentration. *Chem. Geol.* 400, 44–55.
- Price, F.T., Shieh, Y.N., 1979. Fractionation of sulfur isotopes during laboratory synthesis of pyrite at low temperatures. *Chem. Geol.* 27 (3), 245–253.
- Rickard, D., Luther, G.W., 2007. Chemistry of Iron Sulfides. *Chem. Rev.* 107 (2), 514–562.
- Rickard, D., Luther, III, G.W., 1997. Kinetics of pyrite formation by the  $\text{H}_2\text{S}$  oxidation of iron (II) monosulfide in aqueous solutions between 25 and 125 °C: the mechanism. *Geochim. Cosmochim. Acta* 61 (1), 135–147.
- Ries, J.B., Fike, D.A., Pratt, L.M., Lyons, T.W., Grotzinger, J.P., 2009. Super-heavy pyrite ( $\delta^{34}\text{S}_{\text{pyr}} > \delta^{34}\text{S}_{\text{CAS}}$ ) in the terminal Proterozoic Nama Group, Southern Namibia: a consequence of low seawater sulfate at the dawn of animal life. *Geology* 37 (8), 743–746.
- Rio, D., Channell, J.E.T., Massari, F., Poli, M.S., Sgavetti, M., D’Alessandro, A., Prosser, G., 1996. Reading Pleistocene eustasy in a tectonically active siliciclastic shelf setting (Crotona peninsula, southern Italy). *Geology* 24 (8), 743–746.
- Risgaard-Petersen, N., Revil, A., Meister, P., Nielsen, L.P., 2012. Sulfur, iron-, and calcium cycling associated with natural electric currents running through marine sediment. *Geochim. Cosmochim. Acta* 92, 1–13.
- Robinson, B.W., 1995. IAEA-TECDOC-825, 39–45.
- Roda, C., 1964. Distribuzione e facies dei sedimenti Neogenici del Bacino Crotonese. *Geol. Romana* 3, 319–366.
- Rossi, S., Sartori, R., 1981. A seismic reflection study of the external Calabrian Arc in the northern Ionian Sea (eastern Mediterranean). *Mar. Geophys. Res.* 4, 403–426.
- Rossi, V., Azzarone, M., Capraro, L., Faranda, C., Ferretti, P., Macrì, P., Scarponi, D., 2018. Dynamics of benthic marine communities across the Early-Middle Pleistocene boundary in the Mediterranean region (Valle di Manche, Southern Italy): Biotic and stratigraphic implications. *Palaeogeogr. Palaeoclimatol. Palaeoecol.* 495, 127–138.
- Scarponi, D., Huntley, J.W., Capraro, L., Raffi, S., 2014. Stratigraphic paleoecology of the Valle di Manche section (Crotona Basin, Italy): a candidate GSSP of the Middle Pleistocene. *Palaeogeogr. Palaeoclimatol. Palaeoecol.* 402, 30–43.
- Sim, M.S., Bosak, T., Ono, S., 2011. Large Sulfur Isotope Fractionation does not require Disproportionation. *Science* 333, 74–77.
- Sweeney, R.E., Kaplan, I.R., 1973. Pyrite framboid formation; laboratory synthesis and marine sediments. *Econ. Geol.* 68 (5), 618–634.
- Szpak, P., Metcalfe, J.Z., Macdonald, R.A., 2017. Best practices for calibrating and reporting stable isotope measurements in archaeology. *J. Archaeol. Sci. Rep.* 13, 609–616.
- Toth, D.J., Lerman, A., 1977. Organic matter reactivity and sedimentation rates in the ocean. *Am. J. Sci.* 277 (4), 465–485.
- Van Dijk, J.P., 1992. Late Neogene fore-arc basin evolution in the Calabrian Arc (central Mediterranean); tectonic sequence stratigraphy and dynamic geohistory. Ph.D. Thesis. Utrecht University, p. 288.
- Van Dijk, J.P., Okkes, M., 1991. Neogene tectonostratigraphy and kinematics of Calabrian basins; implications for the geodynamics of the Central Mediterranean. *Tectonophysics* 196, 23–60.
- Wan, M., Schroeder, C., Peiffer, S., 2017. Fe(III):S(-II) concentration ratio controls the pathway and the kinetics of pyrite formation during sulfidation of ferric hydroxides. *Geochim. Cosmochim. Acta* 217, 334–348.
- Wang, P., Tian, J., Lourens, L.J., 2010. Obscuring of long eccentricity cyclicity in Pleistocene oceanic carbon isotope records. *Earth Planet. Sci. Lett.* 290 (3–4), 319–330.
- Wing, B.A., Halevy, I., 2014. Intracellular metabolite levels shape sulfur isotope fractionation during microbial sulfate respiration. *Proc. Natl. Acad. Sci.* 111 (51), 18116–18125.
- Yan, D., Chen, D., Wang, Q., Wang, J., Wang, Z., 2009. Carbon and sulfur isotopic anomalies across the Ordovician–Silurian boundary on the Yangtze Platform, South China. *Palaeogeogr. Palaeoclimatol. Palaeoecol.* 297, 32–39.
- Zecchin, M., Caffau, M., Di Stefano, A., Maniscalco, R., Lenaz, D., Civile, D., Muto, F., Critelli, S., 2013. The Messinian succession of the Crotona Basin (southern Italy) II: Facies architecture and stratal surfaces across the Miocene–Pliocene boundary. *Mar. Pet. Geol.* 48, 474.
- Zhang, T., Shen, Y., Zhan, R., Shen, S., Chen, X., 2009. Large perturbations of the carbon and sulfur cycle associated with the late Ordovician mass extinction in South China. *Geology* 37, 299–302.